Geophysical Research Letters

RESEARCH LETTER
10.1029/2018GL080858

Partitioned Off-Fault Deformation in the 2016 Norcia Earthquake Captured by Differential Terrestrial Laser Scanning

L. N. J. Wedmore[1,2], L. C. Gregory[1], K. J. W. McCaffrey[3], H. Goodall[1], and R. J. Walters[4]

[1]Institute of Geophysics and Tectonics, School of Earth and Environment, University of Leeds, Leeds, UK, [2]Now at Department of Earth Sciences, University of Bristol, Bristol, UK, [3]Department of Earth Sciences, Durham University, Durham, UK, [4]COMET, Department of Earth Sciences, Durham University, Durham, UK

Key Points:
- The first known example of an earthquake rupture imaged with preearthquake and postearthquake terrestrial laser scanning
- We differenced the laser scans using an iterative closest point algorithm refined for accurately resolving centimeter-scale offsets
- We find that off-fault deformation is strongly partitioned between the horizontal and vertical components of displacement

Supporting Information:
- Supporting Information S1

Correspondence to:
L. N. J. Wedmore,
luke.wedmore@bristol.ac.uk

Citation:
Wedmore, L. N. J., Gregory, L. C., McCaffrey, K. J. W., Goodall, H., & Walters, R. J. (2019). Partitioned off-fault deformation in the 2016 Norcia earthquake captured by differential terrestrial laser scanning. *Geophysical Research Letters*, *46*, 3199–3205. https://doi.org/10.1029/2018GL080858

Received 10 OCT 2018
Accepted 21 FEB 2019
Accepted article online 27 FEB 2019
Published online 25 MAR 2019

Abstract Field measurements of coseismic fault slip often differ from surface slip models derived from satellite geodesy. Quantifying these differences is challenging as many geodetic techniques inadequately image near-fault deformation. We use an iterative closest point algorithm to difference preearthquake and postearthquake terrestrial laser scanning point clouds to reveal centimeter-scale patterns of surface deformation caused by shallow fault slip in the 2016 M_w 6.6 Norcia (Central Italy) earthquake. Terrestrial laser scanning offsets are constant along the fault and match average field measurements. Eighty-four percent of vertical displacement occurs on a discrete fault zone, with 16% of deformation distributed across a narrow zone <4 m wide. In contrast, horizontal deformation is distributed over an 8-m-wide zone with approximately 50% of extension accommodated as off-fault deformation (OFD). The centimeter-scale observation of deformation shows that horizontal and vertical coseismic OFD is partitioned—in this case, OFD is dominated by horizontal deformation.

Plain Language Summary During an earthquake, slip on a fault plane creates discrete offsets at depth and at the surface. The pattern and size of offsets at the surface can help to understand what happened in the earthquake and also leaves a record of each event in the landscape. This record is used to infer past earthquake activity and forecast the potential likelihood of future earthquakes. We captured a preearthquake image of a fault that caused the 2016 magnitude 6.6 Norcia earthquake in Central Italy. By reimaging the same fault after the earthquake, we measured the pattern of ground movement during the event to millimeter precision to understand in unprecedented detail how much earthquake slip occurs on the fault itself. This uniquely precise map of surface deformation has never been captured before using a terrestrial laser scanner. We find that the vertical motion of the fault is mainly focused on the fault itself. In contrast, the horizontal motion is distributed over an 8-m-wide zone, with approximately 50% of the movement occurring away from the fault—known as *off-fault deformation*. Our results have implications for how evidence of past earthquakes preserved in the landscape are interpreted for forecasting future seismic hazard.

1. Introduction

Most evidence for preinstrumental earthquakes comes from paleoseismic trenches and geomorphic observations of fault offsets collected in the few meters surrounding a fault zone. Observations of earthquakes from satellite geodesy have shown that slip in the shallow subsurface often differs considerably from the magnitude and pattern of slip on the deeper portions of the fault (the shallow slip deficit; Fialko et al., 2005). Whether this discrepancy is due to shallow fault zone mechanics is unclear due to limitations of satellite geodetic techniques for resolving surface fault breaks (e.g., Wright et al., 2003). Regardless, there is a fundamental lack of observations of the 3-D displacement field of shallow fault zone slip, aside from field-based measurements of fault rupture that are generally only able to record offset across discrete surface ruptures (see Brooks et al., 2017; Rockwell & Klinger, 2013, for exceptions). Consequently, it is unclear how offsets recorded in paleoseismic trenches relate to slip in the deeper portions of a fault zone, and the energy and moment release of the seismic events that the paleo-offsets represent is therefore uncertain. We examine the shallow fault zone behavior during the M_w 6.6 2016 Norcia earthquake in Central Italy, which we imaged by differencing preseismic and postseismic terrestrial laser scanning (TLS) data sets.

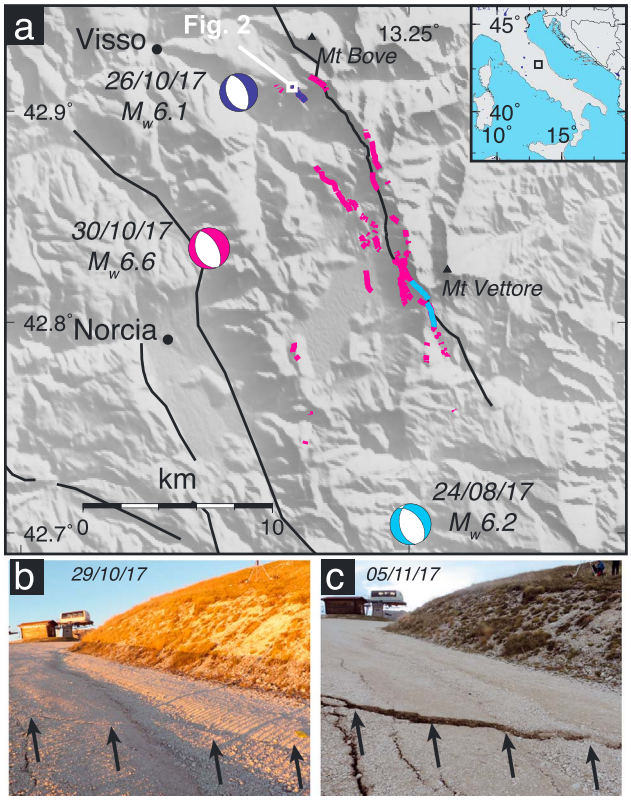

Figure 1. (a) Map of the central Apennines, Italy, showing the location of the events in the 2016 Central Italy earthquake sequence and the study area (focal mechanisms are composite geodetic solutions from Walters et al., 2018, with locations from Chiaraluce et al., 2017). Surface ruptures for the M_w 6.2 (light blue) and M_w 6.1 (dark blue) earthquakes were both reruptured and overprinted by the M_w 6.6 earthquake (magenta). The offset between the focal mechanism and the surface ruptures of the M_w 6.2 earthquake is due to the complex rupture of the earthquake that spanned two faults: The Mt. Vettore fault, (shown here) and the Laga fault to the south. (b) The study site 12 hr before the M_w 6.6 Norcia earthquake showing the small approximately1-cm offset caused by the M_w 6.1 Visso earthquake. (c) The study site following the M_w 6.6 Norcia earthquake.

High-resolution optical imagery and airborne lidar can capture near-fault earthquake surface deformation that is invisible to other geodetic techniques. For example, while interferometric synthetic aperture radar has revolutionized how we are able to constrain earthquake slip, the loss of coherence along surface ruptures means that it is not always possible to accurately model both surface and subsurface displacement. Using iterative closest point (ICP) algorithms to difference preearthquake and postearthquake airborne lidar data can reveal near fault deformation (e.g., Nissen et al., 2014). However, this technique requires window sizes that exceed approximately 20 by 20 m in order to reduce the errors (Nissen et al., 2012)—larger than the scale at which paleoseismic and surface slip observations are often made. Similarly, cross-correlation methods on high-resolution optical imagery can operate on submeter scale pixels (e.g., Barnhart et al., 2015; Vallage et al., 2015) but can suffer from biases and artifacts introduced by using smoothed surfaces or gridded digital elevation model's during processing (Ayoub et al., 2009), and the technique can only resolve slip in earthquakes with large, meter-scale displacements. Differenced TLS data sets can help bridge this gap by imaging fault displacement in exceptionally high resolution (>100 points per square meter), allowing better insight into the faulting process (e.g., Wilkinson et al., 2010). To date, preseismic and postseismic TLS data sets of an earthquake surface rupture have not been available for comparison.

We present TLS observations of near-field fault slip from a section of fault that ruptured in the 2016 Central Italy earthquake sequence. The sequence featured three $M > 6$ earthquakes over a period of 3 months that combined to rupture the Mt. Vettore-Mt. Bove fault system (Figure 1; Walters et al., 2018). On 29 October 2016, we collected TLS data on a section of the Mt. Bove fault that ruptured in the M_w 6.1 Visso earthquake on 26 October 2016. While initially collected as a postearthquake data set, these data became a preearthquake data set for the M_w 6.6 Norcia earthquake that ruptured the same fault segment on 30 October, 12 hr after our first data collection. We returned to the site and collected a postearthquake data set on 5 November (Figure 1). We difference these preearthquake and postearthquake TLS data to document surface deformation caused by shallow fault slip in the Norcia earthquake and map spatial changes in surface deformation to within 0.5 m of the discrete surface rupture. We compare both vertical and horizontal deformation at a range of scales from field measurements collected on the surface rupture to ICP displacements at distances of <1, 4, and 8 m from the fault. This enables us to identify differences between discrete deformation associated with the surface rupture and off-fault distributed deformation at a range of distances from the fault. We find significant off-fault deformation (OFD) occurs in <8-m-wide zones surrounding the fault, and we show that the OFD is strongly partitioned into its horizontal and vertical components.

Table 1
Details of the Terrestrial Laser Scans Collected in This Study

Scan	Location[a]		Date collected	Frequency (MHz)	Number of points[b]
	X UTM (m)	*Y* UTM (m)			
Preearthquake					
Scan position 1	351022	4752698	2016-10-29	350	247,756,037
Postearthquake					
Scan position 1	351022	4752698	2016-11-05	350	156,286,117
Scan position 2	351059	4752642	2016-11-05	350	6,364,068

[a]WGS 1984, UTM zone 33T. [b]Prior to manual filtering and application of 5-cm spatial filter.

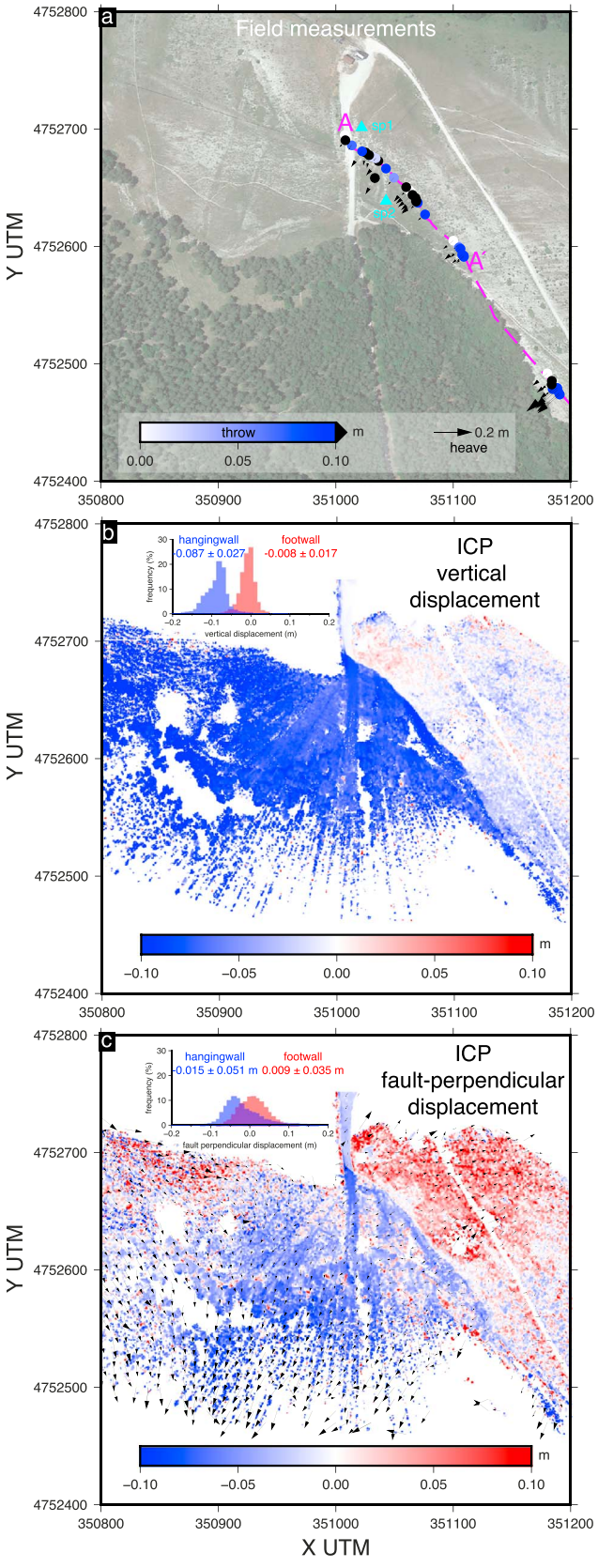

2. Methods

2.1. Field Data Collection

TLS is a ground-based active remote sensing method that is able to collect large volumes of 3-D point cloud data (10^2–10^4 points per square meter; Table 1 and Figure S2 in the supporting information). We used a RIEGL VZ-1000 terrestrial laser scanner to collect both preearthquake and postearthquake TLS data surrounding a section of the Mt. Bove fault during the 2016 Central Italy earthquake sequence (Figures 1 and 2). The preearthquake scan was globally referenced using three registration targets in the footwall of the fault that were surveyed using a differential Global Navigation Satellite System. For the postearthquake scan, two different scan position data sets were internally tied together using the same preearthquake registration target positions. Initial point cloud processing was carried out using RiSCAN Pro (v 2.4). Due to deformation and tilting of the footwall during the earthquakes, the postearthquake point cloud was precisely referenced to a portion of the footwall close to the fault by using a point-to-point ICP algorithm within Cloud Compare (see supporting information). We manually removed return ambiguities caused by distant topography and applied a spatial filter to remove points closer than 5 cm to each other in Cloud Compare; no other filtering of the raw point clouds was applied.

2.2. Point Cloud Differencing

To difference the preearthquake and postearthquake point clouds, we used a windowed point-to-plane ICP algorithm within MATLAB that iteratively calculates the rigid body transformation that minimizes the sum of the squared differences between windows of the preevent point cloud, which are fixed, and windows of the postearthquake point cloud (Bouaziz et al., 2013; Chen & Medioni, 1992; Nissen et al., 2017). The resulting transformation matrix contains three components of displacements (t_x, t_y, and t_z) as well as rotations about the x, y, and z axes. While this method has been previously used on airborne lidar (e.g., Nissen et al., 2012, 2014, 2017), we carried out synthetic tests on the preearthquake point cloud to determine the ability of the ICP method to resolve displacements using TLS data and to refine the workflow (see supporting information). These tests show that the ICP method can accurately resolve vertical displacements on the order of centimeters close to the fault (Figures S3–S14). However, close to the surface rupture, the ICP algorithm is unable to precisely fit a rigid body transformation using just the three components of translation and consequently introduces rotations to minimize the root-mean-square error (Figure S10). The effect and

Figure 2. (a) Google Earth image of the fault section near to Frontignano where we collected a preearthquake and postearthquake terrestrial laser scan. The location and magnitude of the surface rupture is also indicated. (b) ICP vertical displacements from the M 6.6 Norcia earthquake. The inset histogram is plotted with a bin width of 0.01 m, with the hanging wall (blue) and footwall (red) points selected either side of the distinct offset observed in the ICP vertical displacement field. (c) ICP horizontal displacements. The arrows show the vectors of the horizontal displacement (see part a for scale). The underlying colors are the horizontal displacements resolved perpendicular to the mean fault strike across the segment. The inset histogram uses the same points as part b to compare the footwall and hanging wall displacements. The ICP displacement field in parts b and c have been gridded at 1-m resolution in this figure. ICP = iterative closest point.

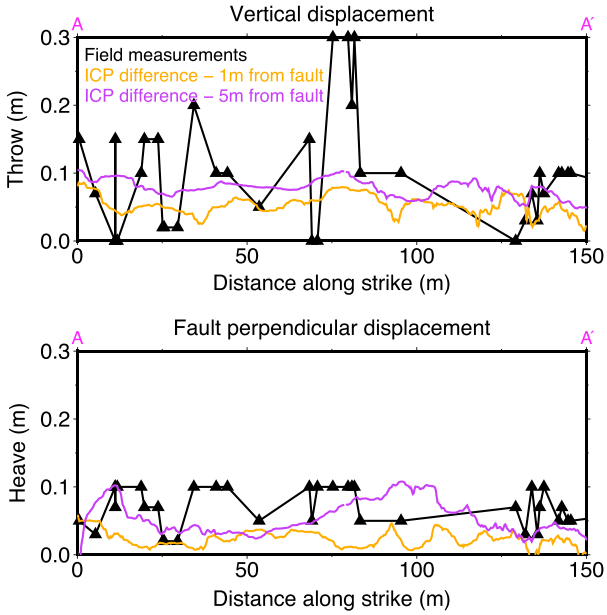

Figure 3. Along-strike ICP results and field measurements. The field measurements were collected using measuring tapes, rulers, and compass clinometers with matching points identified on either side of the fault to precisely measure throw, heave, and slip direction (Villani et al., 2018). The field measurements are plotted alongside the median difference between the footwall and hanging wall ICP results at 1 and 5 m from the fault calculated in 25-cm sections along strike. ICP = iterative closest point.

extent of these rotations can be reduced by applying a sliding window approach, removing solutions that do not converge, and applying a spatial median filter with a 1-m search radius to the ICP transformation results that has the effect of removing significant outliers (Figures S15 and S18). To difference the preearthquake and postearthquake TLS data using an ICP algorithm, we subdivide the point clouds into local windows of 1 m × 1 m, with an additional buffer zone to account for the horizontal displacement during the earthquake. We used a buffer zone of 0.4 m as this was greater than the largest offset measured without being overly computationally expensive, and it did not curtail the histograms of horizontal displacement (Figure 2c). We applied a sliding window of 0.2 m that leads to an 80% overlap between adjacent cells. The spatial median filter was then applied before we resolved the horizontal displacement vectors t_x and t_y in the direction perpendicular to the mean strike of the fault. We compare the ICP-derived displacements with field measurements collected using conventional field-based methods in the aftermath of the earthquake by the openEMERGEO team (Villani et al., 2018).

3. Results

The hanging wall of the fault was downthrown by 7–10 cm in the earthquake as shown by the vertical ICP displacements that sharply delineate the discrete surface rupture, even in regions with dense tree cover (Figure 2b). In contrast, the horizontal fault-perpendicular displacements show a diffuse transition between the hanging wall and the footwall (Figure 2c). To analyze the difference between the distribution of horizontal and vertical surface displacement (i.e., discrete rupture vs. diffuse deformation), we calculate the difference between the ICP displacement in the footwall and hanging wall measured at 0.5- to 1-m half width distance from the fault, which represents the closest distance from the fault that our ICP method can resolve (see Figure S18), and compare this to the field measurements of surface offset measured on the fault. We also calculate the ICP displacements further away from the fault to estimate the percentage of deformation that is distributed away from the discrete surface rupture.

The vertical ICP displacement calculated by differencing the hanging wall and footwall points within 0.5–1 m of the fault is consistently 5–10 cm along strike (Figure 3a), whereas the field measurements of rupture throw vary significantly along strike between 0 and 30 cm (Figures 2a and 3a). When averaged along the 150-m-long section in Figure 3, the mean throw (and 1σ uncertainty) measured in the field (10 ± 9 cm) is comparable to the mean vertical displacement between the hanging wall and footwall points measured 5 m from the fault trace (7.6 ± 0.1 cm—purple line in Figure 3a). Vertical displacement increases from 6.4 ± 0.1 cm close to the fault (0.5–1 m) to 7.6 ± 0.1 cm 5 m from the fault but is relatively constant (~7.6 cm) beyond 4 m from the fault (Figures 4a and 4c). This equates to ~16% of vertical displacement occurring as OFD, which is restricted to a zone <4 m wide.

Projecting the horizontal displacements into fault perpendicular motion (compare Figure 2c with Figure S19) reveals a more discrete rupture across the fault than the individual orthogonal horizontal components of the ICP results (Figure S19), although the horizontal data are still noisier than the vertical displacements. The dominant motion is perpendicular to the fault strike (arrows in Figure 2c), consistent with the dip-slip motion expected from a normal fault. The mean horizontal motion of the hanging wall is toward 244° ± 35°, and the mean strike of the fault is 139° ± 12° (mean and 1σ). The mean fault heave from the field measurements (7 ± 3 cm) is significantly more than ICP fault perpendicular displacements measured within 1 m from the fault (2.8 ± 0.1 cm) but comparable to the ICP fault perpendicular displacements measured 5 m away from the fault (4.7 ± 0.1 cm; Figure 3b). While the ICP displacements do show a discrete surface rupture, the horizontal displacement also increases significantly with distance away from the fault and only becomes constant (~5.5 cm) beyond 8 m from the fault (Figures 4b and 4d). This equates to ~50% of the horizontal deformation being accommodated as OFD in a distributed manner across an 8-m-wide zone.

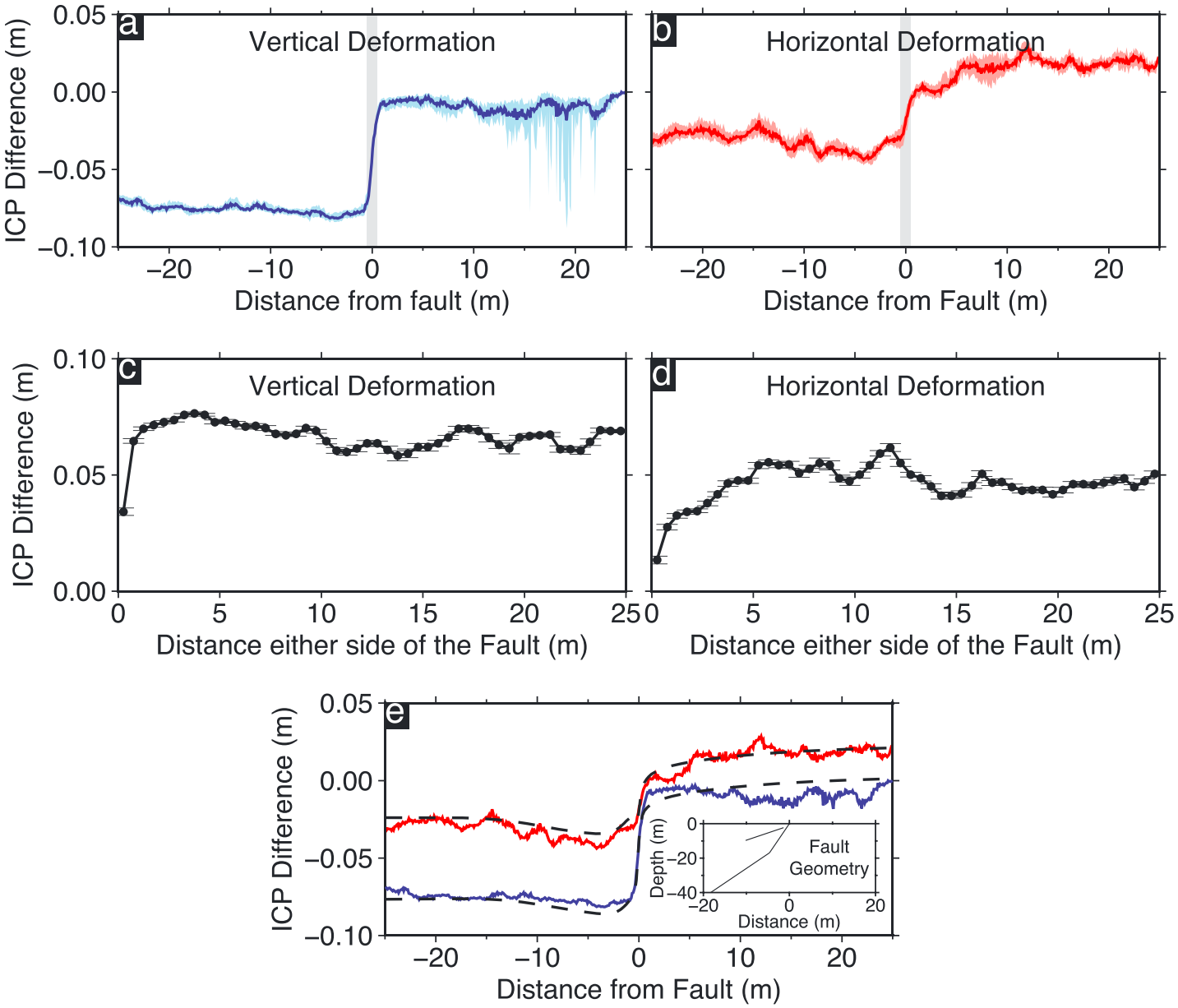

Figure 4. (a) Across-strike bootstrapped medians of the iterative closest point (ICP) vertical displacement between A and A′ in Figure 2a. The light blue area shows the range of medians of the individual bootstrap samples. The thick blue line is the mean of these samples. (b) Across-strike bootstrapped medians of the ICP horizontal displacement between A and A′ in Figure 2a. The light red area shows the range of medians of the individual bootstrap samples. The thick red line is the mean of these samples. (c) The difference between the bootstrapped samples of vertical displacement from the hanging wall and footwall at distances in 0.5-m intervals from the fault. (d) The difference between the bootstrapped samples of horizontal displacement from the hanging wall and footwall at distances in 0.5-m intervals from the fault. (e) Predicted displacements (dashed lines) of horizontal (red) and vertical (blue) ICP displacements from our elastic model (Coleman & Li, 1996; Okada, 1985). The fault geometry is shown in the inset. See supporting information for more information on the modeling.

4. Discussion and Implications

The high spatial resolution of the data set that we collected indicates that both vertical and horizontal ICP displacements show evidence of a discrete surface rupture (Figure 2). The ICP derived offsets close to the fault rupture (0.5–1 m; our method cannot resolve <0.5 m—see supporting information) are generally lower than the field measurements (Figure 3). In contrast, the ICP displacements at greater distances from the fault (4–5 m) are approximately constant along strike and are consistent with the mean of the field measurements within error. A comparison of ICP measurements close to the rupture with those measurements at greater

distances indicates that displacement increases in a diffuse manner across a finite zone due to OFD. This diffuse OFD is not captured in the field measurements reported by Villani et al. (2018) because the magnitude of the diffuse deformation approaches the resolution of field measurements (although errors are not explicitly stated, they are typically on the order of ~5 cm). In general, traditional field measurements struggle to capture an accurate measure of how *wide* this zone of diffuse deformation is and thus the amount of OFD. In contrast, satellite-based geodetic techniques struggle to capture how *narrow* the zone of diffuse deformation is and the nature of the off-fault deformation within the zone. Interferometric synthetic aperture radar is limited by pixel size and incoherence across such narrow zones of faulting—Sentinel-1 interferograms across this section of fault are generally incoherent within at least 1 km of the fault (Walters et al., 2018).

While satellite- and field-based methods are suboptimal for capturing zones of diffuse deformation close to a surface rupture, airborne lidar has proved useful in capturing the 3-D near-fault displacement field. The only other example of ICP displacements calculated in a pure normal faulting earthquake known to us was using airborne lidar on the M_w 7.1 Fukushima-Hamadori earthquake (Nissen et al., 2014). Here they found that the horizontal east-west and north-south ICP displacements were noisy and did not show a discontinuity across the fault rupture, despite a clear vertical signal. We analyze the horizontal displacements in the Norcia earthquake by projecting them into fault perpendicular motion (Figure 2c). While we also find greater noise in the horizontal displacement, we are still able to resolve centimeter-scale features in the displacement field (Figure 4). We suspect the higher noise may be due to generally smooth horizontal surfaces or the difficulty in horizontally matching spatially and temporally variable vegetation cover (although data were filtered for vegetation by Nissen et al., 2014).

By using TLS to capture the displacement field in centimeter-scale resolution, we show that the spatial extent of the zones of horizontal and vertical diffuse OFD varies from ~8 m in the horizontal to ~4 m in the vertical. In addition, ~50% of the horizontal deformation is accommodated in a distributed manner away from the discrete surface rupture whereas only ~16% of vertical deformation occurs away from the discrete fault. This suggests that more of the horizontal extension associated with normal faulting does not reach the surface (compared to the vertical deformation), indicating that the shallow slip deficit here is partitioned. This occurs due to partitioned OFD and can be explained by several potential mechanisms. A simple elastic dislocation model can explain the first-order partitioned deformation field if the fault dip steepens in the shallow subsurface and a shallow synthetic fault and/or antithetic faulting accommodates some deformation in the immediate near field of the primary fault (i.e., <30-m depth and <20-m distance from the primary fault; Figures 4e and S21). Steepening the dip of the fault close to the surface has the effect of disproportionately inducing a near-surface shallow horizontal displacement deficit, while the effect on the vertical displacement field is smaller. Distributed deformation dominated by opening on a network of shallow fractures could also contribute to the partitioned OFD. Despite these models being nonunique and simplistic, they give some indication of potential first-order processes affecting near-fault deformation. Intriguingly, partitioned distributed deformation was also observed by Scott et al. (2018) in the 2016 Kumamoto strike-slip earthquake, but in the opposite sense, with vertical deformation twice as distributed as horizontal deformation. This observation suggests that the orientation of the principal compressive stresses (i.e., σ_1 is vertical for normal faults and horizontal for strike-slip faults) may also play a role in facilitating distributed OFD.

The implications of our results and illustrative modeling are that partitioned OFD could be caused by a combination of changes in near-surface fault geometry and OFD taken up on a diffuse network of faults. Consequently, the total slip in a prehistoric earthquake or cumulative fault scarp may be underestimated if only a narrow fault zone is investigated or if OFD is poorly preserved in the landscape. Overall, this highlights the need for more high-resolution near-fault studies of coseismic deformation.

5. Conclusions

We collected TLS data from a section of the Mt. Vettore-Mt. Bove fault system shortly before and after the M_w 6.6 Norcia earthquake in 2016. Using ICP differencing to calculate coseismic deformation, we find evidence for discrete vertical deformation, with a small component (~16%) of distributed deformation limited to a narrow 4-m-wide zone. In contrast, horizontal extension shows a smaller discrete surface

offset, and ~50% of the extension is accommodated as off-fault distributed deformation over an 8-m-wide zone. These first differential TLS observations of coseismic slip at this scale reveal insights into the partitioning of the coseismic OFD and the nature of distributed shallow slip that are not resolvable using airborne lidar, satellite radar interferometry, or most traditional field surveying techniques.

Acknowledgments
This work was supported by NERC Urgency grant NE/P018858/1 and NERC IRF NE/M019020/1 to LG. The TLS data are available on OpenTopography (https://www.opentopography.org). The preearthquake data are available at https://doi.org/10.5069/G9JQ0Z4H. The postearthquake data are available at https://doi.org/10.5069/G9CV4FV2. We thank Paolo Marco de Martini for his generous assistance with our fieldwork, Eutizio Vittori for alerting us to the surface ruptures of the Visso Earthquake, and Ed Nissen for help with the ICP code. Figures were made using the Generic Mapping Tools (Wessel & Smith, 1998). We thank Mike Oskin, an anonymous reviewer, and the Associate Editor for their helpful reviews that improved this paper.

References

Ayoub, R., Leprince, S., & Avouac, J. P. (2009). Co-registration and correlation of aerial photographs for ground deformation measurements. *ISPRS Journal of Photogrammetry and Remote Sensing*, *64*(6), 551–560. https://doi.org/10.1016/j.isprsjprs.2009.03.005

Barnhart, W. D., Briggs, R. W., Reitman, N. G., Gold, R. D., & Hayes, G. P. (2015). Evidence for slip partitioning and bimodal slip behavior on a single fault: Surface slip characteristics of the 2013 Mw7.7 Balochistan, Pakistan earthquake. *Earth and Planetary Science Letters*, *420*, 1–11. https://doi.org/10.1016/j.epsl.2015.03.027

Bouaziz, S., Tagliasacchi, A., & Pauly, M. (2013). Sparse iterative closest point. *Computer Graphics Forum*, *32*(5), 113–123. https://doi.org/10.1111/cgf.12178

Brooks, B. A., Minson, S. E., Glennie, C. L., Nevitt, J. M., Dawson, T., Rubin, R., et al. (2017). Buried shallow fault slip from the South Napa earthquake revealed by near-field geodesy. *Science Advances*, *3*(7), e1700525. https://doi.org/10.1126/sciadv.1700525

Chen, Y., & Medioni, G. (1992). Object modelling by registration of multiple range images. *Image and Vision Computing*, *10*(3), 145–155. https://doi.org/10.1016/0262-8856(92)90066-C

Chiaraluce, L., di Stefano, R., Tinti, E., Scognamiglio, L., Michele, M., Casarotti, E., et al. (2017). The 2016 Central Italy seismic sequence: A first look at the Mainshocks, aftershocks, and source models. *Seismological Research Letters*, *88*(3), 757–771. https://doi.org/10.1785/0220160221

Coleman, T. F., & Li, Y. (1996). An interior trust region approach for nonlinear minimization subject to bounds. *SIAM Journal on Optimization*, *6*(2), 418–445. https://doi.org/10.1137/0806023

Fialko, Y., Sandwell, D., Simons, M., & Rosen, P. (2005). Three-dimensional deformation caused by the Bam, Iran, earthquake and the origin of the shallow slip deficit. *Nature*, *435*(7040), 295–299.

Nissen, E., Krishnan, A. K., Arrowsmith, J. R., & Saripalli, S. (2012). Three-dimensional surface displacements and rotations from differencing pre- and post-earthquake LiDAR point clouds. *Geophysical Research Letters*, *39*, L16301. https://doi.org/10.1029/2012GL052460

Nissen, E., Malireddi, S.R., Clark, K., Hamling, I., Langridge, R., Ries, W., & Tagliasacchi, A. (2017). Three-dimensional coastal deformation in the Mw7.8 Kaikoura earthquake from differential airborne lidar. Proceedings of the 8th International INQUA Meeting on Paleoseismology, Active Tectonics and Archaeoseismology (Pata), pp. 292–295.

Nissen, E., Maruyama, T., Arrowsmith, J. R., Elliott, J. R., Krishnan, A. K., Oskin, M. E., & Saripalli, S. (2014). Coseismic fault zone deformation revealed with differential lidar: Examples from Japanese Mw ~7 intraplate earthquakes. *Earth and Planetary Science Letters*, *405*, 244–256. https://doi.org/10.1016/j.epsl.2014.08.031

Okada, Y. (1985). Surface deformation due to shear and tensile faults in a half-space. *Bulletin of the Seismological Society of America*, *75*(4), 1135–1154.

Rockwell, T. K., & Klinger, Y. (2013). Surface rupture and slip distribution of the 1940 Imperial Valley earthquake, Imperial fault, Southern California: Implications for rupture segmentation and dynamics. *Bulletin of the Seismological Society of America*, *103*(2A), 629–640. https://doi.org/10.1785/0120120192

Scott, C. P., Arrowsmith, J. R., Nissen, E., Lajoie, L., Maruyama, T., & Chiba, T. (2018). The M7 Kumamoto, Japan, earthquake: 3D deformation along the fault and within damage zone constrained from differential lidar topography. *Journal of Geophysical Research: Solid Earth*, *123*, 6138–6155. https://doi.org/10.1029/2018JB015581

Vallage, A., Klinger, Y., Grandin, R., Bhat, H. S., & Pierrot-Deseilligny, M. (2015). Inelastic surface deformation during the 2013 Mw 7.7 Balochistan, Pakistan, earthquake. *Geology*, *43*, 1079–1082.

Villani, F., Civico, R., Pucci, S., Pizzimenti, L., Nappi, R., De Martini, P., & Open EMERGEO Working Group (2018). A database of the coseismic effects following the 30 October 2016 Norcia earthquake in central Italy. *Scientific Data*, *5*, 180049. https://doi.org/10.1038/sdata.2018.49

Walters, R. J., Gregory, L. C., Wedmore, L. N. J., Craig, T. J., McCaffrey, K., Wilkinson, M., et al. (2018). Stop-start seismic sequences and rupture complexity in continental fault networks. *Earth and Planetary Science Letters*, *500*, 1–14. https://doi.org/10.1016/j.epsl.2018.07.043

Wessel, P., & Smith, W. H. (1998). New, improved version of generic mapping tools released. *Eos, Transactions American Geophysical Union*, *79*(47), 579. https://doi.org/10.1029/98EO00426

Wilkinson, M., McCaffrey, K. J. W., Roberts, G., Cowie, P. A., Phillips, R. J., Michetti, A. M., et al. (2010). Partitioned postseismic deformation associated with the 2009 Mw 6.3 L'Aquila earthquake surface rupture measured using a terrestrial laser scanner. *Geophysical Research Letters*, *37*, L10309. https://doi.org/10.1029/2010GL043099

Wright, T. J., Lu, Z., & Wicks, C. (2003). Source model for the Mw 6.7, 23 October 2002 Nenana Mountain earthquake (Alaska) from InSAR. *Geophyiscal Research Letters*, *30*(18), 1974. https://doi.org/10.1029/2003GL018014